Review

Ultrafast synthesis of electrocatalysts

Qiming Liu[1] and Shaowei W. Chen [1],*

Carbon-based nanocomposites have been hailed as low-cost, high-performance electrocatalysts that may rival precious metal-based commercial benchmarks in a range of electrochemical energy technologies, such as fuel cells, water electrolyzers, and metal–air batteries. These materials are typically prepared by thermal treatment of select precursors at elevated temperatures, such as controlled pyrolysis and hydro/solvothermal methods, which are time-consuming and energy-intensive. Recently, effective techniques have been developed for the ultrafast synthesis of such electrocatalysts based on the Joule effect, microwave irradiation, laser ablation, and magnetic induction heating, which markedly reduce the amount of time and energy in sample preparation and more significantly, produce nonequilibrium structures that are unattainable in conventional procedures, leading to unprecedented electrocatalytic performances.

Trends in ultrafast synthesis

Design and engineering of low-cost, high-performance electrocatalysts represent a critical first step in the advancement of important electrochemical energy technologies, such as fuel cells, water electrolyzers, and metal–air batteries, thanks largely to the complex reaction pathways and sluggish electron-transfer kinetics of the cathode and anode reactions [1]. Whereas precious metal-based materials are the catalysts of choice for these reactions, carbon-based nanocomposites have recently emerged as viable alternatives with their reduced costs and competitive performances. These composites are generally prepared by thermal treatment of select precursors at elevated temperatures, such as controlled pyrolysis and hydro/solvothermal procedures, which are time and energy intensive [2]. Recently, effective techniques have been developed for the **ultrafast synthesis** (see Glossary) of such functional nanocomposites [3,4], based on **carbothermal shock, flash Joule heating** (FJH) [5–7], **microwave irradiation** [8–10], **laser ablation** [11], **magnetic induction heating** (MIH) [12,13], **flame synthesis** [14–16], **plasma sputtering** [17,18], and **electrosynthesis** [19], among others. In these ultrafast procedures, the samples can be prepared within milliseconds to seconds, and the materials structures may exhibit a clear deviation from the thermodynamic equilibrium that is manifested in the traditional **time-temperature-transformation diagram**, in sharp contrast to those derived from conventional synthesis [7,20]. In fact, immiscibility of metals can be overcome allowing the formation of unprecedented alloys. In addition, because of the short heating duration, mobility and aggregation of atomic species are significantly impeded [12,19], leading to the formation of rampant structural defects, such as **stacking faults**, **twin boundaries**, **dislocations**, **Schottky defects**, and **Frenkel defects** [21–25]. Such nonequilibrium features may play a critical role in dictating the interactions with key reaction intermediates and the eventual electrocatalytic activity.

In this review, we first summarize recent advances in the ultrafast synthesis of novel electrocatalysts by thermal shock, FJH, laser ablation, microwave irradiation, and MIH (Box 1); highlight the unique materials structures and the relevant electrocatalytic performances toward important electrochemical reactions; and finally, include a perspective for future research.

Highlights

Several methods have been developed for the ultrafast synthesis of materials, including thermal shock, flash Joule heating, microwave irradiation, laser ablation, magnetic induction heating, flame pyrolysis, and plasma sputtering.

A range of electrocatalysts have been prepared by ultrafast methods and exhibited unprecedented catalytic activity and selectivity toward important reactions in electrochemical energy technologies, due largely to the formation of nonequilibrium structures, such as defects, vacancies, and metastable phases, which are unattainable in sample preparation based on wet chemistry and conventional thermal procedures.

Ultrafast synthesis significantly reduces the preparation time and can be exploited for large-scale sample preparation and high-throughput sample screening. This is a critical step in activity optimization of desired electrocatalysts.

[1]Department of Chemistry and Biochemistry, University of California, 1156 High Street, Santa Cruz, CA 95064, USA

*Correspondence:
shaowei@ucsc.edu (S.W. Chen).

Check for updates

Box 1. Introduction on and comparison of ultrafast synthetic techniques

Carbothermal shock and FJH are both based on the Joule heating effect, which use conductive carbon materials as the substrates and can reach a high temperature within milliseconds, rendering the decomposition of precursors. Laser ablation uses a high-energy pulsed laser as the heating source, with a high heating and cooling rate, creating a high temperature at a small spot on the material surface, leading to local decomposition or ablation of the targets. Microwave irradiation uses electromagnetic irradiation to induce structural changes in target materials, where control of the resulting temperature is challenging. MIH uses a high-frequency electromagnetic field to generate noncontact Eddy currents on the metal pieces and thermal-radiatively decompose the target precursors with a high heating and cooling rate. Flame synthesis utilizes flame combustion to burn the precursors on select substrates, which are usually used to prepare metal oxides and carbon-based materials. Electroshock method, a way of electrosynthesis on a relatively low scale, deposits metals onto ultramicroelectrodes within milliseconds by electrochemical reduction of metal ions. Moving bed pyrolysis uses a traditional furnace as the heating apparatus, where the sample can be physically moved out of the heating zone, which greatly reduces the time of sample preparation by removing the long heating duration and annealing process. The comparison of these techniques is summarized in Table I.

Table I. Comparison of various ultrafast synthetic techniques

Synthetic techniques	Energy resources	Time scale	Temperature range
Carbothermal shock	Direct currents	Within milliseconds	Up to thousands of Kelvin
FJH	Discharge from capacitors	Within milliseconds	Up to thousands of Kelvin
Laser ablation	High-energy pulsed laser beams	From milliseconds to minutes (for accumulation of materials)	Up to thousands of Kelvin locally
Microwave irradiation	Electromagnetic irradiation	From seconds to minutes	Up to 1000 K, but usually implicit
MIH	Eddy current generated by electromagnetic fields	Within seconds, can last longer to minutes if needed	Up to 1800 K, depends on the heating metal
Flame synthesis	Flame combustion	Within seconds	Up to thousands of Kelvin, but nonuniform
Electroshock method	Electrochemical reduction	Within milliseconds	Room temperature
Plasma sputtering	Plasma bombard reaction	Within tens of seconds	From room temperature to hundreds of Kelvin
Moving bed pyrolysis	Regular tube furnaces	Within minutes	Up to 1000 K

Thermal shock

Carbothermal shock can be exploited to heat conductive samples up to thousands of Kelvin at high direct currents within milliseconds (**Joule's law**), leading to a drastic transformation of the structures of materials. For instance, microparticles of Al, Si, Sn, Au, and Pd supported on reduced graphene oxide (rGO) can be readily converted into nanoparticles of about 10 nm by applying a high direct current for 2 ms (Figure 1A,B), due to thermal shock (ca. 1700 K) that melted the starting particles into smaller ones [26]. The procedure was also used to convert Ni microparticles on rGO into Ni nanoparticles of about 75 nm encapsulated by thin carbon layers [27], which exhibited a remarkable electrocatalytic activity toward the electrooxidation of H_2O_2 (602 mA cm^{-2} at +0.2 V vs. Ag/AgCl), a performance 150 times higher than that of the original Ni microparticles. In a similar fashion, metal chalcogenide (e.g., FeS_2) nanoparticles were produced on rGO by thermal shock of micron-sized precursors at about 2470 K followed by **quenching** to room temperature within 12 ms (Figure 1C) [28]. The obtained FeS_2/rGO composites exhibited an excellent electrocatalytic activity toward the hydrogen evolution

Glossary

Carbothermal shock: using a direct current to generate a high temperature on conductive carbon within milliseconds and thermally decompose precursors into target materials.

Dislocation: line defects in a crystal structure, with an abrupt change in the linear arrangement of atoms.

Electrosynthesis: electrochemical synthesis of materials.

Flame synthesis: using flame combustion to manufacture materials, typically metal oxides or carbon-based materials.

Flash Joule heating: heating carbon to a high temperature within milliseconds by using a high current generated by high-voltage electric charge from a capacitor bank.

Frenkel defect: a point defect in crystals where an atom (or ion) leaves its original site and occupies an interstitial site.

High-entropy alloy: alloys produced by the mixing of at least five metal elements at comparable proportions.

Joule's law: the amount of heat (Q) produced when an electric current (I) is passed through a conductor (resistance R) for a specific period of time (t) is equal to $Q = I^2Rt$.

Laser ablation: removing materials from the surface by using a high-energy laser beam.

Linear scaling correlation: the linear relations between the binding energies of various critical reaction intermediates on active sites, which may have opposite effects on the reaction kinetics and hence catalytic activity.

Magnetic induction heating: using an alternating electromagnetic field to generate a high current on conductive materials, which can heat the materials to an elevated temperature within seconds.

Microwave irradiation: exposing materials to strong electromagnetic irradiation in the microwave frequency range produces a high heat and rapidly transforms the material structures.

Overpotential: the difference between applied potential and equilibrium potential in an electrochemical half-reaction.

Plasma sputtering: a plasma-based process where atoms are bombarded off a target material and deposited onto a substrate.

Quenching: rapid cooling of materials in a medium after thermal treatment.

reaction (HER) in acidic media, with an **overpotential** ($\eta_{HER,10}$) of −139 mV to reach the current density of 10 mA cm^{-2}, much lower than that of the micro-sized ones (−260 mV), due to the manipulation of the chemical composition and structure of the nanoparticles and their interactions with the rGO substrate. When thermal shock was applied to carbon nanofibers coated with PdCl$_2$ and NiCl$_2$ at 1550 K for 1 s, the salts were decomposed into PdNi nanoparticles with abundant twin boundaries and stacking faults [25]. Such unique structural features were difficult to produce in traditional synthetic methods, resulting in an excellent activity toward HER ($\eta_{HER,10}$ = −86.3 mV) and H$_2$O$_2$ electrooxidation. Excellent HER activities in alkaline media were also observed with thermal shock-derived IrNi nanoalloy and Pt nanoparticles (Figure 1D) [29,30].

Thermal shock even enables localized high-temperature (ca. 1400 K) synthesis under extreme conditions, such as in liquid nitrogen (ca. 77 K; Figure 1D), where the fast quenching facilitates the formation of strains within the nanoparticles. In fact, Pt nanoparticles synthesized in liquid nitrogen (Dr-Pt) possessed abundant dislocations (Figure 1E,F), and the strong strain effects (Figure 1G) impacted the adsorption of H* species. By contrast, Pt particles synthesized in ambient Ar (Dp-Pt) did not exhibit many dislocations, and the HER activity was markedly lower (Figure 1H). The Dr-Pt nanoparticles also displayed excellent stability (Figure 1I). Similarly, thermal shock has been used to synthesize NiO with O vacancies [31] and Pd nanoparticles with twin boundaries [32] for the electrocatalytic oxidation of methanol, ethylene glycol, and ethanol.

Thermal shock can also be exploited to overcome the thermodynamic immiscibility between metal elements [7,33]. For instance, Cu is immiscible with most transition metals, and phase segregation typically occurs in bimetallic systems (Figure 1J). Yet, it has been demonstrated that thermal shock of a mixture of Cu–X salts (X = Ag, Ni, Sn, In, Pd) on carbon nanofibers at 1300°C for 0.2 s produced Cu–X nanoalloys (ca. 16 nm) with a homogenous phase (Figure 1K,L) [33]. For comparison, phase segregation was observed for particles prepared at 1000°C with a conventional furnace, and the size was much larger at 100–500 nm. Monte Carlo simulations showed that the nonequilibrium bimetallic mixture was kinetically stable at room temperature. The obtained Cu–X nanoalloys could effectively catalyze the electroreduction of CO into multicarbon products (Figure 1M), and Cu$_{0.9}$Ni$_{0.1}$ showed the highest Faradic efficiency of about 76% at a current density of about 93 mA cm^{-2}, much higher than that of Cu alone. *In situ* attenuated total reflection surface-enhanced infrared absorption spectroscopy measurements showed that Ni alloying strengthened the adsorption of CO on the active sites.

Nanoparticles of **high-entropy alloys** [34], oxides [35,36], sulfides [37], and phosphates [38] have also been readily prepared by thermal shock, exhibiting breaking of the **linear scaling correlation** between the electronic properties and electrocatalytic activities [20,39] that is key to the enhancement and optimization of the electrocatalytic performance, in sharp contrast to samples prepared by traditional methods. For instance, 10-element high entropy oxide nanoparticles with an ultrafine size of 7 nm (10-HEO with Hf, Zr, La, V, Ce, Ti, Nd, Gd, Y, and Pd) were successfully prepared on carbon black by using thermal shock at 1400 K within 1 s (Figure 1N,O) [35], and possessed a much enhanced mass activity (and stability) toward the oxygen reduction reaction (ORR; Figure 1P), as compared with commercial Pd. This was ascribed to the atomic distribution of Pd within the single-phase oxide consisting of the other nine elements, where formation of high-entropy oxides reduced the migration and agglomeration of Pd and thus enhanced the ORR stability.

Notably, multiple samples can be concurrently prepared with thermal shock [40], with a ready control of the elemental composition from binary to octonary. Thermal shock is indeed a powerful

Schottky defect: a point defect in crystals where an atom (or ion) leaves its original site and creates a vacancy.
Stacking fault: a planar defect that breaks the periodic sequence of crystal planes.
**Time-temperature-transformation diagram:** a plot of temperature versus time that describes the phase transformation of materials in a thermal treatment process.
Topotactic transition: a change of the crystallographic structure of a material that may entail a loss or gain of the crystalline solid.
Turnover frequency: the number of molecules transformed within a unit period of time per one active site in a catalytic cycle.
Twin boundary: a grain boundary formed at the interface between two mirror crystal planes, which is a planar defect.
Ultrafast synthesis: sample preparation in a rapid fashion as compared with conventional methods.
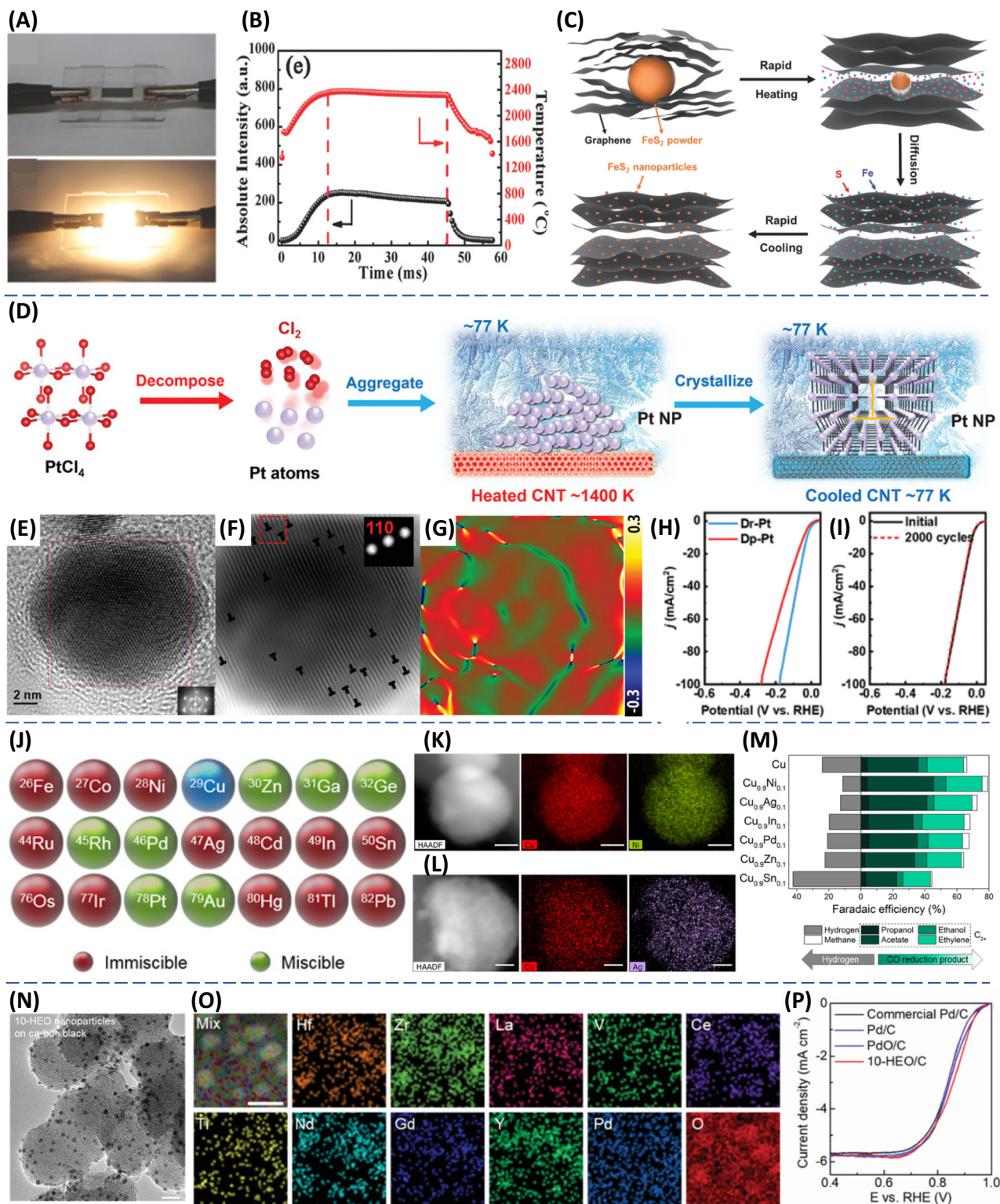
tool in the high-throughput preparation and screening of electrocatalysts, which can be aided by data-driven calculations and machine learning. Further research is desired to explore the application of thermal shock in a controlled atmosphere (e.g., H_2 or CO_2) or in a liquid medium for more deliberate manipulation of the structures of materials.

Flash Joule heating

FJH is another ultrafast heating technique based on high-voltage electric discharge that can be powered with a capacitor bank and generate a temperature over 3000 K under 100 ms (Joule's law), along with an ultrafast cooling rate up to 10^4 K s^{-1}. Such rapid heating and quenching are almost impossible to attain in conventional methods (Figure 2A,B) [6], and can be exploited for the efficient preparation of metastable materials. In one study [41], a simple FJH treatment at a current of 1350 A for hundreds of milliseconds in a mild vacuum transformed commercial bulk 2H-phase MoS_2 and WS_2 into the metallic 1T phase (Figure 2C,D), which is metastable, thermally unfavorable, and difficult to prepare directly by traditional methods [42,43]. This was ascribed to the formation of S vacancies that accumulated excessive negative charges and made the 1T phase kinetically preferred. The obtained 1T phase exhibited a much enhanced HER activity ($\eta_{HER,10}$ = –221 mV), as compared with the pristine 2H MoS_2 (–491 mV; Figure 2E).

Metal/covalent carbides have also been prepared by FJH (Figure 2F,G) [44]. For instance, phase-pure and defective MoC_{1-x} could be readily obtained at select voltages, such as hexagonal β-Mo_2C (30 V), metastable cubic α-MoC_{1-x} (60 V), and hexagonal η-MoC_{1-x} (120 V; Figure 2H). The **topotactic transition** of β-Mo_2C to either α-MoC_{1-x} or η-MoC_{1-x} was mainly driven by the formation of abundant C vacancies (Figure 2I,J). Electrochemically, β-Mo_2C exhibited a much enhanced HER activity in 0.5 M H_2SO_4 ($\eta_{HER,10}$ = –220 mV), as compared to α-MoC_{1-x} (–310 mV) and η-MoC_{1-x} (–510 mV), along with excellent stability (Figure 2K,L).

FJH is also a viable tool to synthesize carbon-based composites [45,46]. Recently, FJH was used as a solvent- and catalyst-free process to prepare heteroatom-doped (i.e., B, N, O, P, and S) flash graphene (FG) within 100–200 ms at about 3000 K [5]. Notably, the S-doped FG showed a high electrocatalytic activity toward ORR in the 4-e pathway in alkaline media, with a half-wave potential ($E_{1/2}$) of about +0.77 V versus reversible hydrogen electrode (RHE), whereas the 2-e pathway and hence H_2O_2 production were preferred with N-doped FG. Notably, the synthesis could be scaled up to 1 t per day.

Overall, while still at an early stage for catalyst preparation, FJH is a low-cost and powerful method to produce novel electrocatalysts, even on a large scale. Nevertheless, the FJH operation is rather complex, which requires interdisciplinary knowledge of both electrical engineering and chemistry. Meanwhile, FJH requires the addition of conductive materials (e.g., graphene and metals) into the precursors, which may lead to the formation of byproducts and/or impurities.

Figure 1. Ultrafast thermal shock. (A) Digital photographs of the Joule heating device before and during heat treatment. (B) Processed temperature values for the spectra along with the intensity on the 858-nm channel. Reproduced, with permission, from [27]. (C) Schematic illustration of the ultrafast, *in situ* transformation of minerals to catalyst nanoparticles (NPs). Reproduced, with permission, from [28]. (D) Schematic diagram of the preparation of dislocation-rich Pt NPs by thermal shock. (E) High-resolution transmission electron microscopy image of the Dr-Pt NP (scale bar 2 nm), (F) corresponding inverse fast Fourier transform of (110) plane, and (G) strain distribution related to (110) plane. (H) Hydrogen evolution reaction activity and (I) durability evaluation of Dr-Pt. Reproduced, with permission, from [29]. (J) Miscibility of Cu with other metals. Elemental mappings of (K) $Cu_{0.9}Ni_{0.1}$ and (L) $Cu_{0.9}Ag_{0.1}$. Scale bars 5 nm. (M) Faraday efficiency of pure Cu and different $Cu_{0.9}X_{0.1}$ bimetallic catalysts at –0.70 ± 0.01 V versus reversible hydrogen electrode (RHE) toward the electrocatalytic reduction of CO. Reproduced, with permission, from [33]. (N) Transmission electron microscopy image and (O) elemental mapping images of the (Hf, Zr, La, V, Ce, Ti, Nd, Gd, Y, Pd)O_{2-x} NPs supported on the carbon black substrate. Scale bars are (N) 20 nm and (O) 10 nm. (P) Linear sweep voltammetry curves of commercial 5 wt% Pd/C, 22 wt% Pd, 22 wt% PdO, and 22 wt% 10-HEO NPs dispersed on carbon black, tested in an O_2-saturated 0.1 M KOH electrolyte at a potential scan rate of 20 mV s^{-1} and a rotation rate of 1600 rpm. Reproduced, with permission, from [35].
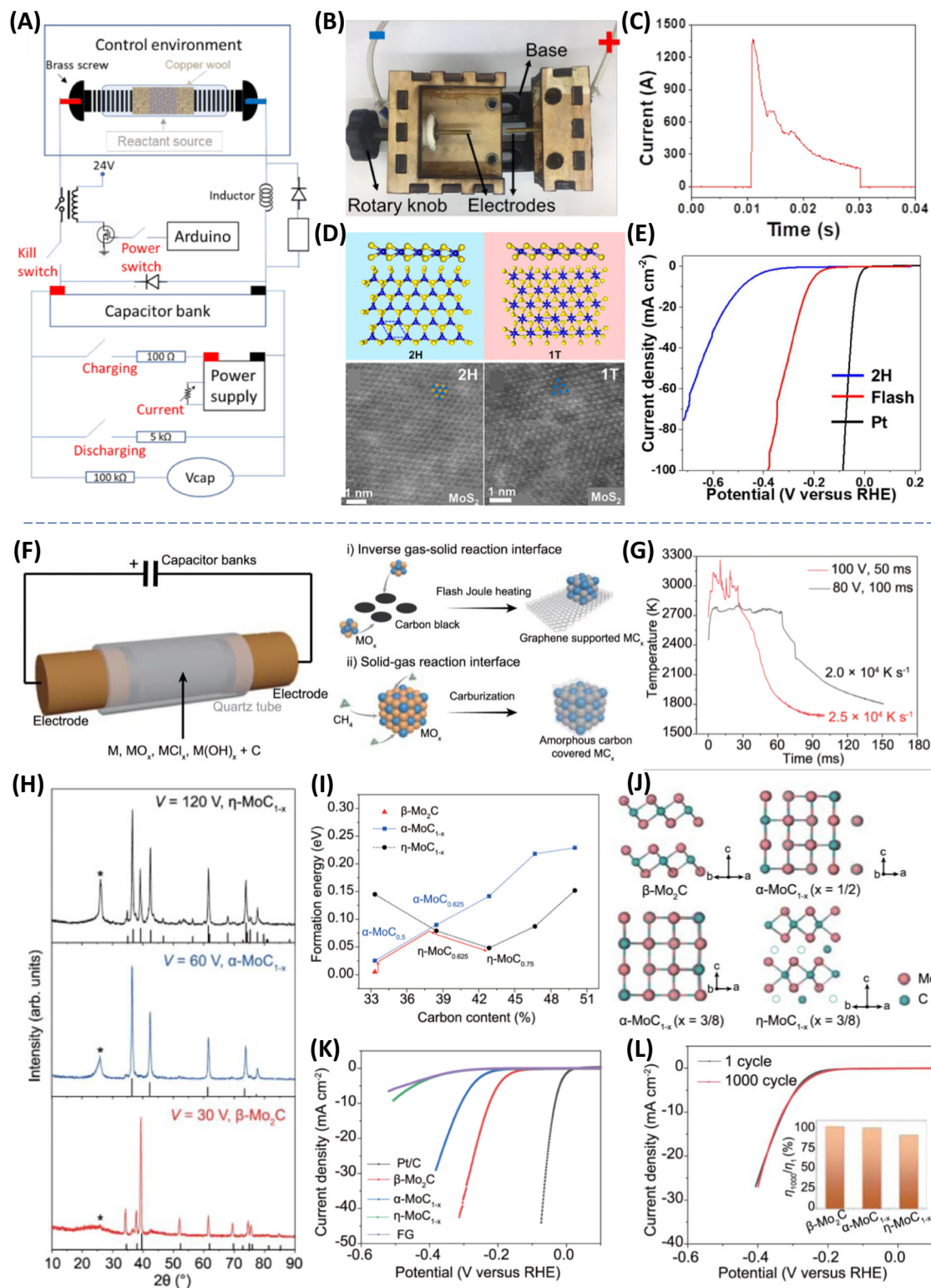
Laser ablation

Laser ablation, based on a nanosecond/picosecond pulse laser, has been used to prepare a range of materials, with a heating/cooling rate up to 10^9 K s^{-1} [47], such as nanoalloys [23,24,48,49], metal oxides [50,51], hydroxides [22,52,53], carbides [54–56], nitrides [57], and chalcogenides [21,58]. In these studies, unique material structures can be produced. For instance, dense stacking faults were observed with Ag nanoparticles (L-Ag) prepared by laser ablation in liquid by shining a pulsed Nd:YAG laser (pulse width 7 ns) on a bulk Ag target in deionized water (Figure 3A,B), where quenching by the surrounding cool water facilitated the formation of abundant vacancies on Ag(111) facets and stacking faults (Figure 3C,D) [24]. The obtained L-Ag nanoparticles displayed an $\eta_{HER,10}$ of only –32 mV in 0.5 M H_2SO_4, significantly lower than that for samples synthesized by conventional wet chemistry (–450 mV), and even slightly better than that of commercial Pt/C (–35 mV; Figure 3E). This was because the stacking faults of L-Ag lowered the Ag coordination number from 12 to 8 and enhanced H adsorption. Laser ablation in liquid was also performed on a bulk Ru target in an Au salt solution to produce Au single-atom alloys of Ru, which exhibited an $\eta_{HER,10}$ of only –24 mV in alkaline media [49], due to fast quenching by the solvent that helped freeze the mobile atoms and create a metastable structure. Note that Ru and Au are immiscible, and it is challenging to synthesize RuAu alloys in traditional methods [59]. Laser ablation of other targets, such as bulk MoS_2 [60] and $CoNi_2P$ [61], have also yielded high-performance electrocatalysts for water splitting.
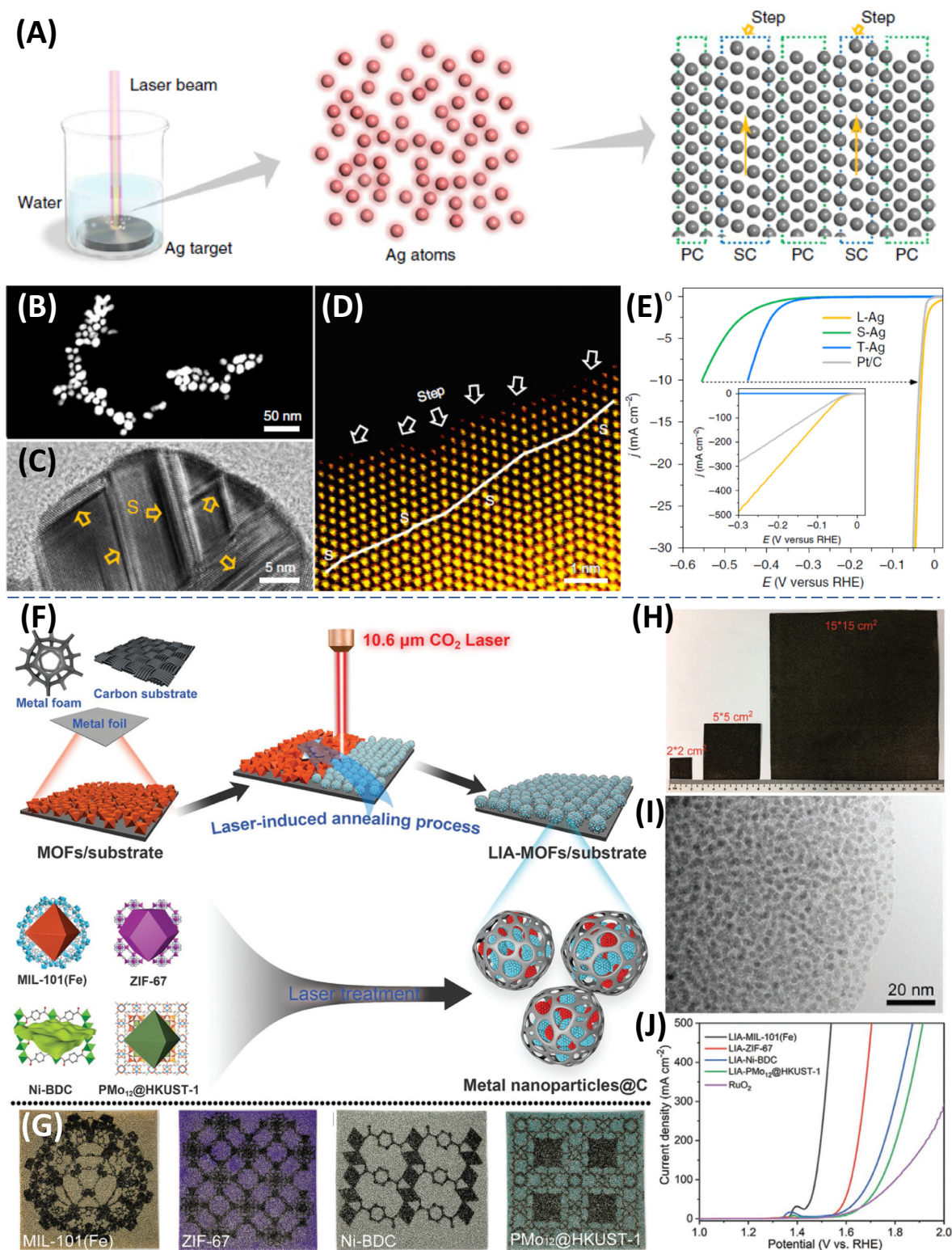
Laser ablation has also been used to pyrolyze select materials into efficient electrocatalysts. For example, Tang and colleagues [62] used a CO_2 laser to pyrolyze metal–organic frameworks supported on various substrate (e.g., nickel foam, carbon cloth), such as ZIF-67, MIL-101(Fe), and Ni-BDC, producing metal nanoparticles encapsulated within a thin carbon shell (NPs@C) in a short time (Figure 3F,G). A large sample surface (up to 15 × 15 cm^2) could be readily prepared by controlling the ablation path (Figure 3H,I). The best sample [MIL-101(Fe) on Ni foam] displayed a low overpotential ($\eta_{OER,50}$) of +225 mV at 50 mA cm^{-2} toward the oxygen evolution reaction (OER) in 1 M KOH (Figure 3J). Efficient OER and ORR electrocatalysts have also been prepared by laser ablation of Kapton polyimide films [63], carbon fiber paper [64], metal-complex-containing polyimide films [65], and metal-immersed cedar woods [66], among others.

Indeed, laser ablation has been used extensively to produce effective electrocatalysts. Because of the high energy and fast quenching rate, it provides a promising route to synthesize metastable electrocatalysts. Nevertheless, laser ablation requires rather expensive apparatus, and the sample productivity is relatively low.

Microwave irradiation

Microwave irradiation can generate an oscillating electric field, electrical dipole, and/or charge, and induce molecular frictions and collisions in target materials, where the kinetic energies can

Figure 2. Catalysts prepared by flash Joule heating (FJH). (A) Circuit diagram of the FJH setup. (B) Photograph of the FJH reaction box. (C) Current versus time profile during the FJH process. (D) Atomic structures of the 2H and 1T phases and the corresponding transmission electron microscopy (TEM) images of the 2H MoS$_2$ precursors and FJH-prepared 1T MoS$_2$. Scale bars 1 nm. (E) HER polarization curves of 2H MoS$_2$, flash MoS$_2$ and commercial Pt/C. Reproduced, with permission, from [41]. (F) Schematic of FJH synthesis of carbides. (G) Real-time temperature measurement by fitting the blackbody radiation from the sample during the FJH process. (H) X-ray diffraction patterns of β-Mo$_2$C, α-MoC$_{1-x}$, and η-MoC$_{1-x}$ synthesized at 30, 60, and 120V, respectively. (I) Formation energy of β-Mo$_2$C, and α-MoC$_{1-x}$ and η-MoC$_{1-x}$ at different carbon atomic contents. (J) Calculated crystal structures of β-Mo$_2$C, α-MoC$_{1-x}$ ($x = 1/2$), α-MoC$_{1-x}$ ($x = 3/8$), and η-MoC$_{1-x}$ ($x = 3/8$). (K) Hydrogen evolution reaction (HER) polarization curves of the three phases of molybdenum carbide and Pt/C and pure flash graphene in 0.5 M H$_2$SO$_4$. (L) HER polarization curves of the first and thousandth cycles of β-Mo$_2$C in 0.5 M H$_2$SO$_4$. Inset shows the ratios of $\eta_{HER,10}$ in the thousandth cycle versus those in the first cycle for β-Mo$_2$C, α-MoC$_{1-x}$, and η-MoC$_{1-x}$. Reproduced, with permission, from [44]. Abbreviation: RHE, reversible hydrogen electrode.

(A)

Laser beam

Water

Ag target

Ag atoms

Step   Step

PC   SC   PC   SC   PC

(B)

50 nm

(C)

S

5 nm

(D)

Step

S
S
S
S

1 nm

(E)

L-Ag
S-Ag
T-Ag
Pt/C

j (mA cm^{-2})

E (V versus RHE)

(F)

Metal foam   Carbon substrate

Metal foil

10.6 μm CO$_2$ Laser

Laser-induced annealing process

MOFs/substrate   LIA-MOFs/substrate

MIL-101(Fe)   ZIF-67

Ni-BDC   PMo$_{12}$@HKUST-1

Laser treatment

Metal nanoparticles@C

(G)

MIL-101(Fe)   ZIF-67   Ni-BDC   PMo$_{12}$@HKUST-1

(H)

15*15 cm^2

5*5 cm^2

2*2 cm^2

(I)

20 nm

(J)

LIA-MIL-101(Fe)
LIA-ZIF-67
LIA-Ni-BDC
LIA-PMo$_{12}$@HKUST-1
RuO$_2$

Current density (mA cm^{-2})

Potential (V vs. RHE)

Trends in Chemistry

*(See figure legend at the bottom of the next page.)*

be converted into heat producing a temperature up to 1000 K [8,10]. The heating rate of microwave ranges from tens to even thousands of K s^{-1}, which depends on several parameters, such as the microwave power and reaction pressure of the machine, as well as target materials morphology, size, loss factor, conductivity, and even structural defects [8,10,67,68]. Microwave-assisted synthesis was first reported in 1986 for organic synthesis [69], and has ever since been extended to the rapid synthesis of a range of materials, such as carbon derivatives [10,70–74], metal/alloy nanoparticles [67,68,75,76], high-entropy alloys/oxides [77,78], metal oxides/hydroxides/nitrides [78–81], metal chalcogenides [82–85], and even single-atom catalysts (SACs) [9,86–88].

For example, graphene-supported SACs were successfully prepared by microwave irradiation of a mixture containing amine-modified graphene oxide, CoCl$_2$, and trace graphene (as a catalyst) at 1000 W for only 5 s (Figure 4A) [9]. Bright flashes were observed (Figure 4B), signifying the production of a high (though unknown) temperature, which facilitated the reduction of amine-modified graphene oxide and N doping into the graphene nanosheets forming N-doped graphene (NG). Meanwhile, the diffusion of metal atoms was impeded by the structural defects and carbon vacancies generated during the heating, leading to immobilization of the metal species and formation of abundant Co single atoms on NG (Figure 4C,D). The Co single atoms were found to possess a relatively low oxidation state and a distorted symmetry of D$_{4h}$, and surrounded by defective graphene, a clear deviation from the atomic configuration of perfect CoN$_4$C$_4$ or Co(II)Pc [cobalt(II) phthalocyanine]. The obtained Co-NG composites exhibited a relatively low $\eta_{HER,10}$ of −175 mV in 0.5 M H$_2$SO$_4$ and a high **turnover frequency** of 0.385 s^{-1} (Figure 4E), whereas Co SACs prepared by prolonged heating in a conventional furnace consisted of CoN$_4$ moieties and exhibited a much lower turnover frequency of only 0.104 s^{-1} [89].

The ORR activity can also be impacted by the generation of imperfect coordination structures of SACs by microwave irradiation [88]. For instance, for Co–N–C composites prepared by microwave irradiation (Figure 4F,G) [90], the formation of low-coordinated CoN$_2$ moieties led to a high selectivity of two-electron ORR with a 90% efficiency of H$_2$O$_2$ production at +0.7 V versus reversible hydrogen electrode (Figure 4H,I), whereas only 50% for CoN$_4$ SACs obtained conventionally (Figure 4J).

Nanoalloys of originally immiscible metals can also be prepared by microwave irradiation. For instance, a variety of Pt–M (M = lanthanide elements of La, Gd, Tb, Er, Tm, and Yb) bimetallic nanoalloys have been prepared by microwave irradiation on Ketjen black [91]. Note that alloying with lanthanide elements is extremely challenging because of their highly negative reduction potentials (typically over −2.0 V), which makes it difficult to reduce them into metallic form even by H$_2$ [92,93]. Yet, when Pt(acac)$_2$ and lanthanide nitrates were mixed together with Ketjen black in a quartz tube, microwave irradiation for only 30 s yielded nanoparticles of 3 nm in diameter with a homogeneous distribution of both Pt and lanthanide (Figure 4K,L), and Pt$_{61}$La$_{39}$ exhibited an even better HER activity in 0.5 M H$_2$SO$_4$ ($\eta_{HER,10}$ = −38 mV) than

Figure 3. Laser ablation in liquid and pyrolysis. (A) Schematic illustration of the synthesis and structure of L-Ag nanoparticles (NPs) by laser ablation in liquid. (B–D) Representative transmission electron microscopy (TEM) images of L-Ag NPs. The yellow open arrows denote stacking faults. Scale bars are (B) 50 nm, (C) 5 nm, and (D) 1 nm. (E) Hydrogen evolution reaction (HER) polarization curves of L-Ag, S-Ag, T-Ag, and Pt/C in 0.5 M H$_2$SO$_4$ at a scan rate of 5 mV s^{-1}. Inset shows the corresponding polarization curves at higher current densities. Reproduced, with permission, from [24]. (F) Schematic illustration of laser-induced annealing of metal–organic frameworks (MOFs) on conductive substrates. (G) Laser-induced annealing of different MOFs into patterns of their corresponding structures on nickel foam (NF). (H) Views of different sizes of MIL-101(Fe) on NF after the laser treatment. (I) TEM image of LIA-MIL-101(Fe). Scale bar 20 nm. (J) Oxygen evolution reaction (OER) polarization curves of LIA-MIL-101(Fe), LIA-ZIF-67, LIA-Ni-BDC, LIA-PMo12@HKUST-1, and commercial RuO$_2$ catalyst in 1 M KOH. Reproduced, with permission, from [62]. Abbreviations: PC, perfect crystal; SC, stacking fault crystal.
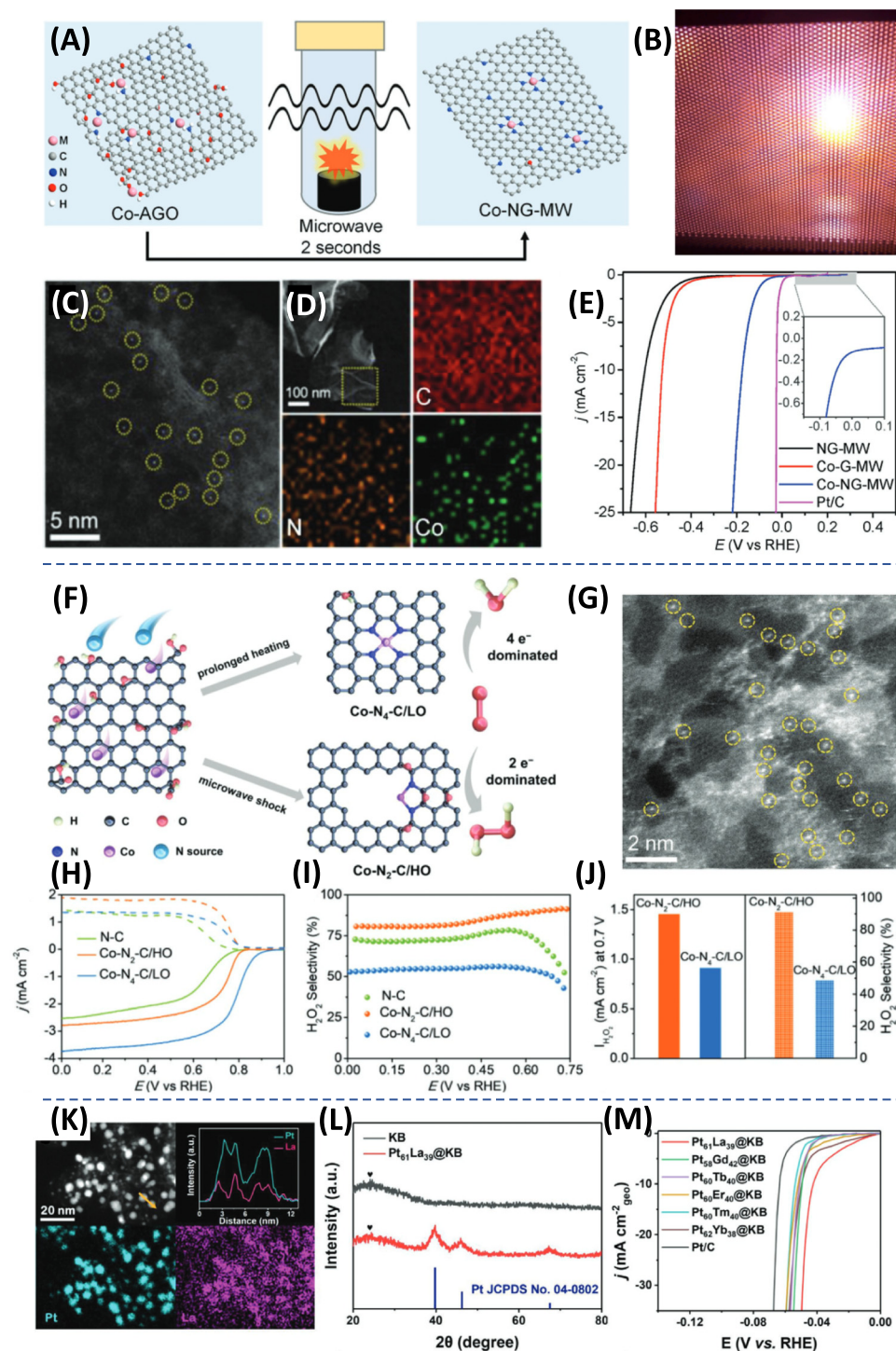
Figure 4. Microwave irradiation synthesis of electrocatalysts. (A) Schematic illustration of the preparation route to Co-NG-MW. (B) Photograph of microwave irradiation. (C) Transmission electron microscopy (TEM) image and (D) elemental maps of Co-NG-MW. Scale bars are (C) 5 nm and (D) 100 nm. (E) Hydrogen evolution reaction (HER)

(Figure legend continued at the bottom of the next page.)

commercial Pt/C (–64 mV) (Figure 4M). This was accounted for by the optimal adsorption energy of H* (–0.017 eV) when Pt was alloyed with La. Meanwhile, the vacancy formation energy of outermost Pt in the $Pt_{61}La_{39}$ alloy was markedly higher than that of pristine Pt, which suppressed the dissolution of Pt and enhanced the stability. Ru–metal carbide (M_xC, M = Mo, Co, Cr) composites supported on carbon nanotubes were also synthesized by using microwave irradiation to pyrolyze metal carbonyl salts within 100 s [94]. The as-prepared Ru–Mo_2C showed an $\eta_{HER,10}$ of only –15 mV in alkaline media, owing to the strong metal–support interactions. Notably, the synthesis could be scaled up to over 1 g, much larger than that based on a tube furnace.
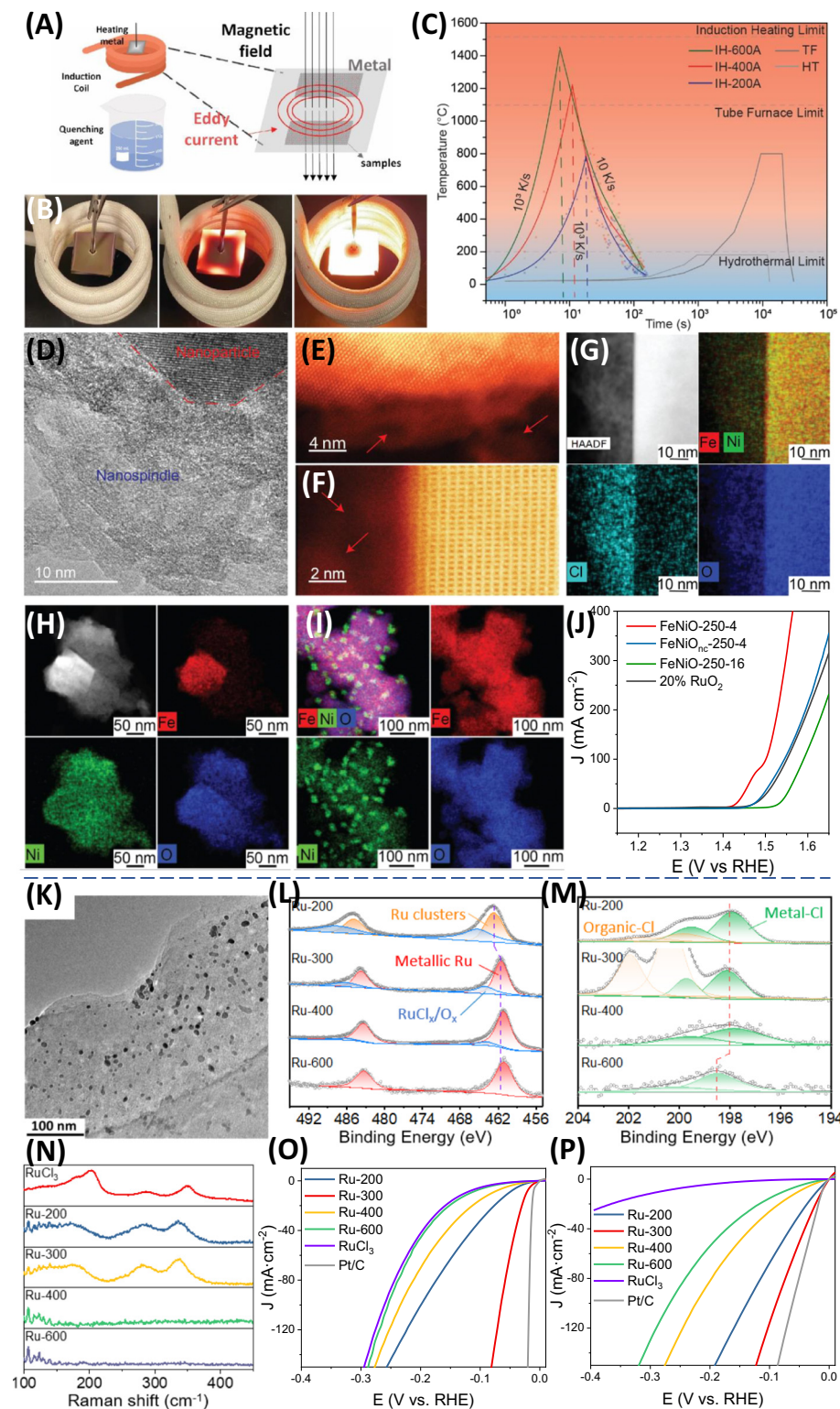
In summary, microwave irradiation can reduce the sample preparation time and yield unconventional structures. As microwave irradiation is readily accessible and low-cost, it may be integrated into other traditional methods, such as ball milling and hydrothermal treatment, as well as be combined with other ultrafast methods, such as laser or Joule heating, for further control of the materials structure and activity. Yet, control of heating temperature is challenging, and the heating rate is relatively low.

Magnetic induction heating

MIH, a traditional metallurgical tool, is a new addition to the ultrafast synthesis of functional materials. Upon the application of a magnetic field, an Eddy current can be generated on the metal surface, thus almost instantly heating the surface to a very high temperature within seconds, due to the Joule heating [95]. MIH has been used for heat management in the thermal catalytic synthesis of graphene [96,97]. Nevertheless, applications of MIH for electrocatalyst preparation have been scarcely reported thus far.

Recently, Chen and colleagues [12,13] used MIH to prepare high-performance OER and HER electrocatalysts for water splitting. In one study [12], $FeCl_3$ and $NiCl_2$ salts were deposited onto carbon paper, which was sandwiched between two thin iron sheets. The assembly was placed in the center of an induction solenoid. Upon the application of a high-frequency (30 kHz) current to the solenoid, a strong magnetic field was produced, rapidly heating up the sample assembly (Figure 5A,B), where the heating temperature could be readily controlled by the applied currents and heating time (Figure 5C). At the end of the heating, the assembly might be dropped into a beaker containing dry-ice cold ethanol (–78°C) for rapid quenching (Figure 5A). Experimentally, at the applied current of 250 A for a heating time of 4 s, the obtained sample (FeNiO-250-4) was found to contain FeNi spinel oxides with a homogeneous mixing of the Fe and Ni phases, and the surface was decorated with Cl-enriched Fe–Ni oxide nanospindles (Figure 5D,G). Such unique structural features were difficult to produce in conventional methods based on 'tedious' thermal treatment. Notably, segregation of the Fe and Ni phases and a large loss of Cl occurred under the identical experimental conditions but without quenching (FeNiO$_{NC}$-250-4; Figure 5H). In addition, when the heating time was prolonged to 16 s, very fine metallic Ni particles were formed on the surface of Fe oxides (FeNiO-250-16; Figure 5I). That is, the materials structures can be effectively manipulated by the applied

polarization curves of Co-NG-MW along with control samples of NG-MW, Co-G-MW, and Pt/C at the scan rate of 5 mV s^{-1} in 0.5 M H_2SO_4. Reproduced, with permission, from [9]. (F) Schematic diagram of the synthesis route to Co-N$_4$-C/LO and Co-N$_2$-C/HO. (G) TEM image of Co-N$_2$-C/HO. Scale bar 2 nm. (H) Rotating ring-disk electrode voltammograms of Co-N$_2$-C/HO, Co-N$_4$-C/LO, and N-C in O_2-saturated 0.1 M KOH. (I) H_2O_2 selectivity on Co-N$_2$-C/HO, Co-N$_4$-C/LO, and N-C. (J) Comparison of H_2O_2 current and H_2O_2 selectivity at +0.7 V for Co-N$_2$-C/HO and Co-N$_4$-C/LO. Reproduced, with permission, from [90]. (K) TEM elemental mapping images and line scans of $Pt_{61}La_{39}$@KB. Scale bar 20 nm. (L) X-ray diffraction patterns of $Pt_{61}La_{39}$@KB. (M) HER polarization curves of Pt-M nanoalloys and commercial Pt/C in 0.5 M H_2SO_4 electrolyte. Reproduced, with permission, from [91]. Abbreviation: RHE, reversible hydrogen electrode.

current, heating time, as well as quenching, and a nonequilibrium structure can be produced by a deliberate regulation of these variables. Electrochemically, the FeNiO-250-4 sample stood out as the best catalyst toward OER in alkaline media among the sample series, displaying an unprecedented performance with an overpotential ($\eta_{OER,100}$) of only +260 mV to reach the high current density of 100 mA cm^{-2} (Figure 5J). This was ascribed to the rapid heating and quenching (ca. 10^3 K s^{-1}) that impeded the phase segregation of the Fe and Ni phases in the spinels and retention of Cl species on the nanospindle surface. Both contributed to the remarkable OER activity, as confirmed in density functional theory calculations.
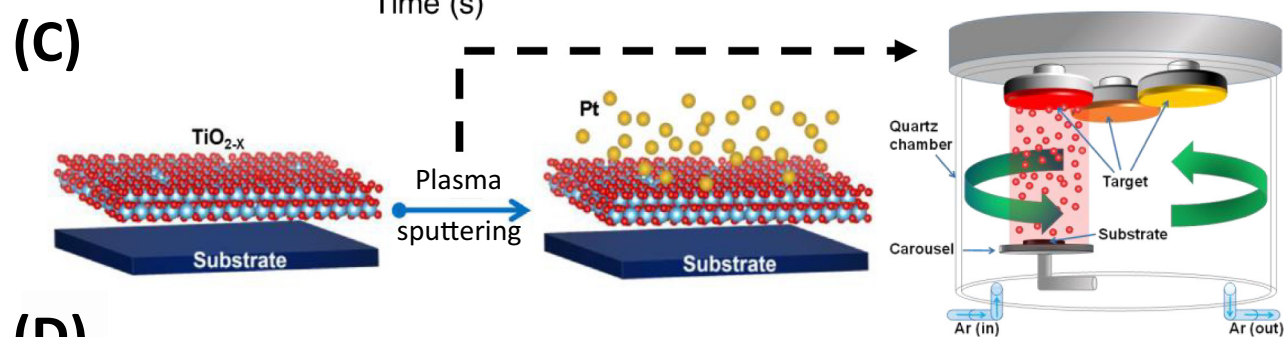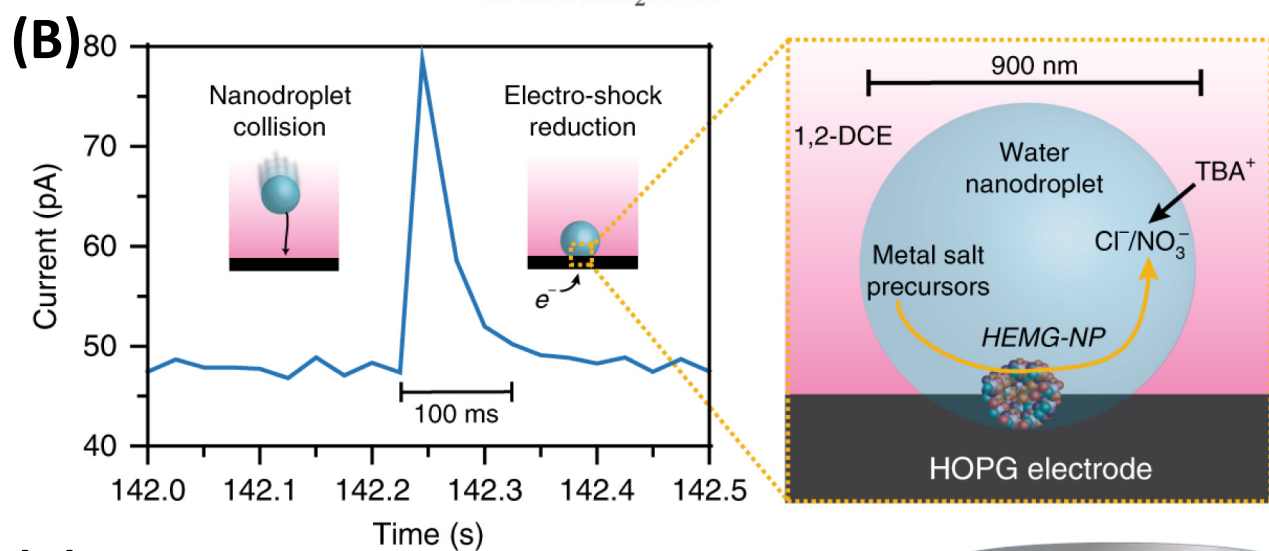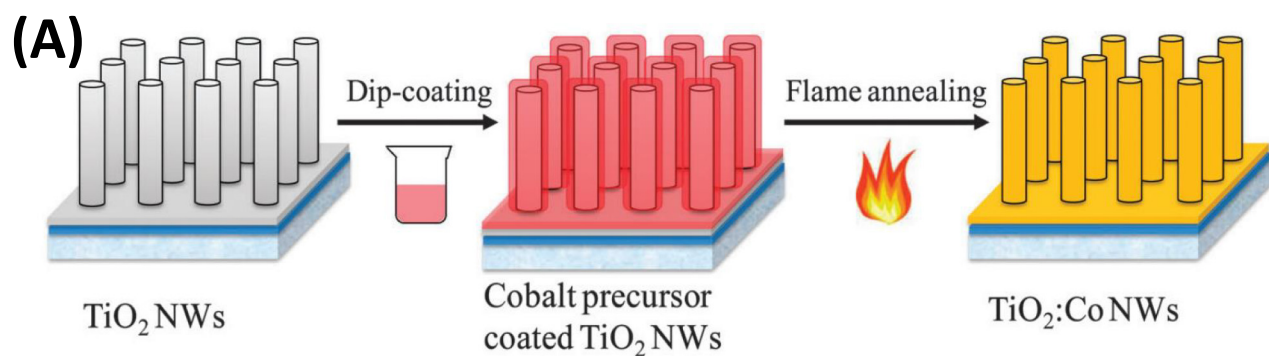
MIH can also be exploited for the rapid preparation of metal nanoparticles supported on carbon derivatives with unique surface chemistry. In another recent study [13], MIH treatment of RuCl$_3$ deposited on carbon paper for just 6 s at 300 A followed by quenching in dry ice/ethanol led to the formation of Ru nanoparticles (average diameter ca. 7 nm, Ru-300; Figure 5K), where the nanoparticle surface was decorated with abundant Cl species, as confirmed in X-ray photo-electron spectroscopy (Figure 5L,M) and Raman measurements (Figure 5N). The content of the surface Ru–Cl species diminished markedly after prolonged heating and/or with an increasing heating current. Remarkably, the Ru-300 sample displayed an ultrahigh HER activity in both acidic ($\eta_{HER,10}$ = –23 mV) and alkaline conditions (–12 mV), clearly outperforming others in the sample series (Figure 5O,P). Results from density functional theory calculations showed that the surface Ru–Cl species facilitated the charge transfer and downshift of the Ru d-band center, and hence optimized the H adsorption on Ru.

Overall, while at an embryonic stage, MIH is an efficient thermal-radiative technique for ultrafast sample preparation. A diverse range of materials can be prepared by MIH, such as metal chalcogenides, carbides, nitrides, and high-entropy alloys [12], due largely to the ready control of the heating temperature (up to 2000 K) by the induction current and frequency.

Other methods

Ultrafast synthesis of electrocatalysts has also been explored by using other energy sources such as flame, electricity, and plasma. For instance, flame has been used to synthesize various OER and HER catalysts, such as Co-doped WS$_2$ [15], copper ferrite [14], and Co-doped TiO$_2$ [16] (Figure 6A). The synthesis typically took minutes and could generate unique features, such as core–shell structures, defects, and meta-1T phases, that might be beneficial to electrocatalysis. Glasscott and colleagues [19] used an electro-shock method (Figure 6B) to synthesize high-entropy metallic glass nanoparticles (HEMG-NPs, from unary to even

Figure 5. Electrocatalysts prepared by magnetic induction heating. (A) Schematic illustration of magnetic induction heating–quenching for material preparation. (B) Photographs of induction heating with a solenoid current at (left) 200 A, (middle) 400 A, and (right) 600 A for 4 s. (C) Variations of temperature versus time of magnetic induction heating, traditional hydrothermal heating, and pyrolysis. The dashed lines indicate the cases with the quenching process. 'IH', 'TF', and 'HT' are short for induction heating, tube furnace, and hydrothermal, respectively. (D) Transmission electron microscopy (TEM) image of nanospindles in FeNiO-250-4. Scale bar 10 nm. (E and F) High-angle annular dark field–scanning transmission electron microscopy (HAADF–STEM) images of nanospindles on the edge of FeNiO-250-4 (low-contrast regions), as highlighted by red arrows. Scale bars are (E) 4 nm and (F) 2 nm. (G) Energy-dispersive X-ray spectroscopy (EDS) mapping images of the interface between nanospindles and nanoparticles in FeNiO-250-4, which show a Cl-rich surface of the nanospindles. Scale bars 10 nm. EDS mapping images of (H) FeNiO$_{NC}$-250-4 and (I) FeNiO-250-16. Scale bars are (H) 50 nm and (I) 100 nm. (J) OER polarization curves of FeNiO-250-4, FeNiO$_{NC}$-250-4, FeNiO-250-16, and 20% RuO$_2$ in 1 M KOH. Reproduced, with permission, from [12]. (K) TEM image of Ru-300 prepared by magnetic induction heating. Scale bar 100 nm. X-ray photoelectron spectroscopy spectra of (L) Ru 3p electrons and (M) Cl 2p electrons of Ru–X (X = 200, 300, 400, 600). (N) Raman spectra of Ru–X and RuCl$_3$. Hydrogen evolution reaction (HER) polarization curves of Ru–X and RuCl$_3$ in (O) 0.5 M H$_2$SO$_4$ and (P) 1 M KOH. Reproduced, with permission, from [13]. Abbreviation: RHE, reversible hydrogen electrode.

(A)

Dip-coating → Flame annealing

TiO₂ NWs → Cobalt precursor coated TiO₂ NWs → TiO₂:Co NWs

(B)

Nanodroplet collision — Electro-shock reduction

100 ms

Current (pA) vs Time (s)

1,2-DCE — 900 nm — Water nanodroplet — TBA⁺ — Cl⁻/NO₃⁻ — Metal salt precursors — HEMG-NP — HOPG electrode

(C)

TiO₂₋ₓ — Substrate → Plasma sputtering → Pt — Substrate

Quartz chamber — Target — Substrate — Carousel — Ar (in) — Ar (out)

(D)

HEA-NPs — Precursors

Trends in Chemistry
(See figure legend at the bottom of the next page.)

octonary) on the surface of carbon fiber ultramicroelectrodes directly for a duration of ca. 100 ms, where the stoichiometric ratios of CoFeLaNiPt HEMG-NPs could be precisely controlled, leading to tunable activity toward electrochemical water splitting. Plasma has also been used to assist rapid synthesis of electrocatalysts [17]. Select materials, such as metal nitrides and single atoms (Figure 6C) that are difficult to synthesize with traditional methods, can be feasibly produced by plasma synthesis within tens of seconds [18,98]. Furthermore, it is worth noting that traditional furnaces can be equipped with a moving bed/reciprocal device (Figure 6D), such that samples can be moved into and out of the high-temperature region at select time points for a precise control of heating and quenching of the samples. This has indeed been demonstrated in the synthesis of high-entropy alloys and SACs toward effective HER and CO_2 reduction [99,100].

Concluding remarks

In summary, ultrafast synthesis of electrocatalysts has been attracting increasing attention, due to the significant reduction of sample preparation time down to even the millisecond level, as compared to at least hours in conventional methods. Such a high time efficiency will be beneficial for the ready expansion of the library of electrocatalysts, and their high-throughput screening and scale-up production. More importantly, ultrafast synthesis can produce nonequilibrium structures that are unattainable with conventional methods and can break the thermodynamic limits for unprecedented electrocatalytic performances. Thus far, several techniques have been demonstrated based on Joule heating, microwave irritation, laser ablation, and magnetic induction, among others, enabling both bottom–up and top–down preparation of a variety of composite catalysts, such as metals, oxides, nitrides, carbides, and chalcogenides. Nevertheless, mechanistic details of how these unique structures are formed have remained mostly elusive. In addition, the complexity of the material structures renders it challenging to correlate the structures of materials (e.g., size, morphology, composition, defect, and phase) with a specific electrocatalytic activity. Further research is strongly desired along these lines (see Outstanding questions). It is anticipated that an intimate integration with *in silico* simulations and *operando* characterizations will yield important insights and empower future research of ultrafast synthesis.

Declaration of interests
No competing interests are declared.

References
1. Ozoemena, K.I. and Chen, S. (2016) *Nanomaterials for Fuel Cell Catalysis. Nanostructure Science and Technology* (1st ed), Springer International Publishing
2. Greeley, J. *et al.* (2006) Computational high-throughput screening of electrocatalytic materials for hydrogen evolution. *Nat. Mater.* 5, 909–913
3. Jiang, R. *et al.* (2021) Ultrafast synthesis for functional nanomaterials. *Cell Rep. Phys. Sci.* 2, 100302
4. Wyss, K.M. *et al.* (2022) Large-scale syntheses of 2D materials: flash Joule heating and other methods. *Adv. Mater.* 34, 2106970
5. Chen, W. *et al.* (2022) Heteroatom-doped flash graphene. *ACS Nano* 16, 6646–6656
6. Luong, D.X. *et al.* (2020) Gram-scale bottom-up flash graphene synthesis. *Nature* 577, 647–651
7. Yao, Y.G. *et al.* (2018) Carbothermal shock synthesis of high-entropy-alloy nanoparticles. *Science* 359, 1489–1494

Outstanding questions

Whereas *in silico* methods such as molecular dynamics can simulate the structural dynamics during the fleeting time of ultrafast synthesis, the relevant experimental confirmation is generally lacking. How can the transient structures be experimentally probed within the short time frame?

Ultrafast syntheses have thus far been conducted in a controlled atmosphere or in liquid. Can the synthesis be extended to solid media, where the relatively rigid spatial confinement may be exploited for further control of the structures of materials?

One unique feature of ultrafast synthesis is the formation of nonequilibrium and metastable structures in the final samples. Do these structures remain stable during the electrochemical reactions? If not, how can one enhance the stability of such thermodynamically unfavorable structures?

The nature of kinetic control in ultrafast synthesis means the formation of an array of complex material structures in the final samples. This poses a significant challenge in the structural correlation with the electrocatalytic activity and ultimately high-throughput screening of the catalysts. Thus, can precise control of material structures be ever achieved in such syntheses?

The toolbox of ultrafast synthesis has remained small thus far. Is it possible to have a select combination of two or more of these techniques for further manipulation of the structures of materials?

Figure 6. Schematics of various ultrafast synthetic methods. (A) Flame synthesis of Co-doped TiO_2. Reproduced, with permission, from [16]. (B) Electrosynthesis of high-entropy glass nanoparticles (NPs). Current transient corresponds to the collision of a single nanodroplet onto a carbon fiber ultramicroelectrode, where nanodroplet contents are fully (>98%) reduced within 100 ms, facilitating disordered co-deposition of various metal precursors. Reproduced, with permission, from [19]. (C) Synthesis of Pt single atoms on TiO_{2-x} by rapid plasma sputtering. Reproduced, with permission, from [18]. (D) Set up of the fast-moving bed for the pyrolytic synthesis of high-entropy alloy (HEA) NPs. Reproduced, with permission, from [99]. Abbreviations: 1,2-DCE, 1,2-dichloroethane; HEMG, high-entropy metallic glass; HOPG, highly ordered pyrolytic graphite; NW, nanowire.

8. Gawande, M.B. *et al.* (2014) Microwave-assisted chemistry: synthetic applications for rapid assembly of nanomaterials and organics. *Acc. Chem. Res.* 47, 1338–1348

9. Fei, H.L. *et al.* (2018) Microwave-assisted rapid synthesis of graphene-supported single atomic metals. *Adv. Mater.* 30, 1802146

10. Schwenke, A.M. *et al.* (2015) Synthesis and modification of carbon nanomaterials utilizing microwave heating. *Adv. Mater.* 27, 4113–4141

11. Zhang, D.S. *et al.* (2017) Laser synthesis and processing of colloids: fundamentals and applications. *Chem. Rev.* 117, 3990–4103

12. Lu, B. *et al.* (2022) Ultrafast preparation of non-equilibrium Fe-Ni spinels by magnetic induction heating for unprecedented oxygen evolution electrocatalysis. *Research* 2022, 9756983

13. Liu, Q. *et al.* (2022) Rapid preparation of carbon-supported ruthenium nanoparticles by magnetic induction heating for efficient hydrogen evolution reaction in both acidic and alkaline media. *SusMat* 2, 335–346

14. Park, S. *et al.* (2019) Rapid flame-annealed CuFe$_2$O$_4$ as efficient photocathode for photoelectrochemical hydrogen production. *ACS Sustain. Chem. Eng.* 7, 5867–5874

15. Shi, X.J. *et al.* (2018) Rapid flame doping of Co to WS$_2$ for efficient hydrogen evolution. *Energy Environ. Sci.* 11, 2270–2277

16. Cai, L.L. *et al.* (2014) Sol-flame synthesis of cobalt-doped TiO$_2$ nanowires with enhanced electrocatalytic activity for oxygen evolution reaction. *Phys. Chem. Chem. Phys.* 16, 12299–12306

17. Dou, S. *et al.* (2018) Plasma-assisted synthesis and surface modification of electrode materials for renewable energy. *Adv. Mater.* 30, 1705850

18. Tian, Y.X. *et al.* (2021) Fast synthesis of Pt single-atom catalyst with high intrinsic activity for hydrogen evolution reaction by plasma sputtering. *Mater. Today Energy* 22, 100877

19. Glasscott, M.W. *et al.* (2019) Electrosynthesis of high-entropy metallic glass nanoparticles for designer, multi-functional electrocatalysis. *Nat. Commun.* 10, 2650

20. Yao, Y. *et al.* (2022) High-entropy nanoparticles: synthesis-structure-property relationships and data-driven discovery. *Science* 376, eabn3103

21. Meng, C. *et al.* (2019) Molybdenum disulfide modified by laser irradiation for catalyzing hydrogen evolution. *ACS Sustain. Chem. Eng.* 7, 6999–7003

22. Meng, C. *et al.* (2019) Laser synthesis of oxygen vacancy-modified CoOOH for highly efficient oxygen evolution. *Chem. Commun.* 55, 2904–2907

23. Wang, H.B. *et al.* (2019) Laser synthesis of iridium nanospheres for overall water splitting. *Materials* 12, 3028

24. Li, Z. *et al.* (2019) A silver catalyst activated by stacking faults for the hydrogen evolution reaction. *Nat. Catal.* 2, 1107–1114

25. Chen, F.J. *et al.* (2018) High-temperature atomic mixing toward well-dispersed bimetallic electrocatalysts. *Adv. Energy Mater.* 8, 1800466

26. Chen, Y.N. *et al.* (2016) Ultra-fast self-assembly and stabilization of reactive nanoparticles in reduced graphene oxide films. *Nat. Commun.* 7, 12332

27. Li, Y.J. *et al.* (2017) *In situ*, fast, high-temperature synthesis of nickel nanoparticles in reduced graphene oxide matrix. *Adv. Energy Mater.* 7, 1601783

28. Chen, Y.N. *et al.* (2017) FeS$_2$ nanoparticles embedded in reduced graphene oxide toward robust, high-performance electrocatalysts. *Adv. Energy Mater.* 7, 1700482

29. Liu, S.L. *et al.* (2022) Extreme environmental thermal shock induced dislocation-rich Pt nanoparticles boosting hydrogen evolution reaction. *Adv. Mater.* 34, 2106973

30. Liu, S.L. *et al.* (2020) Dislocation-strained IrNi alloy nanoparticles driven by thermal shock for the hydrogen evolution reaction. *Adv. Mater.* 32, 2006034

31. Liu, C. *et al.* (2020) Air-assisted transient synthesis of metastable nickel oxide boosting alkaline fuel oxidation reaction. *Adv. Energy Mater.* 10, 2001397

32. Liu, C. *et al.* (2022) Multiple twin boundary-regulated metastable Pd for ethanol oxidation reaction. *Adv. Energy Mater.* 12, 2103505

33. Yang, C.P. *et al.* (2020) Overcoming immiscibility toward bimetallic catalyst library. *Sci. Adv.* 6, eaaz6844

34. Yao, Y.G. *et al.* (2021) Extreme mixing in nanoscale transition metal alloys. *Matter* 4, 2340–2353

35. Li, T.Y. *et al.* (2021) Carbon-supported high-entropy oxide nanoparticles as stable electrocatalysts for oxygen reduction reactions. *Adv. Funct. Mater.* 31, 2010561

36. Dong, Q. *et al.* (2022) Rapid synthesis of high-entropy oxide microparticles. *Small* 18, 2104761

37. Cui, M.J. *et al.* (2021) High-entropy metal sulfide nanoparticles promise high-performance oxygen evolution reaction. *Adv. Energy Mater.* 11, 2002887

38. Qiao, H.Y. *et al.* (2021) A high-entropy phosphate catalyst for oxygen evolution reaction. *Nano Energy* 86, 106029

39. Perez-Ramirez, J. and Lopez, N. (2019) Strategies to break linear scaling relationships. *Nat. Catal.* 2, 971–976

40. Yao, Y. *et al.* (2020) High-throughput, combinatorial synthesis of multimetallic nanoclusters. *Proc. Natl Acad. Sci. USA* 117, 6316–6322

41. Chen, W.Y. *et al.* (2021) Millisecond conversion of metastable 2D materials by flash Joule heating. *ACS Nano* 15, 1282–1290

42. Eda, G. *et al.* (2012) Coherent atomic and electronic hetero-structures of single-layer MoS$_2$. *ACS Nano* 6, 7311–7317

43. Guo, Y.S. *et al.* (2015) Probing the dynamics of the metallic-to-semiconducting structural phase transformation in MoS$_2$ crystals. *Nano Lett.* 15, 5081–5088

44. Deng, B. *et al.* (2022) Phase controlled synthesis of transition metal carbide nanocrystals by ultrafast flash Joule heating. *Nat. Commun.* 13, 262

45. Stanford, M.G. *et al.* (2020) Flash graphene morphologies. *ACS Nano* 14, 13691–13699

46. Algozeeb, W.A. *et al.* (2020) Flash graphene from plastic waste. *ACS Nano* 14, 15595–15604

47. Habiba, K. *et al.* (2014) Fabrication of nanomaterials by pulsed laser synthesis. In *Manufacturing Nanostructures* (Ahmed, W. and Nasar, A., eds), pp. 263–292, One Central Press (OCN)

48. Johny, J. *et al.* (2022) Laser-generated high entropy metallic glass nanoparticles as bifunctional electrocatalysts. *Nano Res.* 15, 4807–4819

49. Chen, C.H. *et al.* (2019) Ruthenium-based single-atom alloy with high electrocatalytic activity for hydrogen evolution. *Adv. Energy Mater.* 9, 1803913

50. Feng, Y. *et al.* (2021) Strawberry-like Co$_3$O$_4$-Ag bifunctional catalyst for overall water splitting. *Appl. Catal. B-Environ.* 299, 120658

51. Zhang, F.F. *et al.* (2021) Iridium oxide modified with silver single atom for boosting oxygen evolution reaction in acidic media. *ACS Energy Lett.* 6, 1588–1595

52. Niu, K.Y. *et al.* (2015) Tuning complex transition metal hydroxide nanostructures as active catalysts for water oxidation by a laser-chemical route. *Nano Lett.* 15, 2498–2503

53. He, G.Y. *et al.* (2022) Laser *in situ* synthesis of NiFe$_2$O$_4$ nanoparticle-anchored NiFe(OH)(x) nanosheets as advanced electrocatalysts for the oxygen evolution and urea oxidation reactions. *Electrochim. Acta* 411, 140074

54. Wu, Y.S. *et al.* (2019) Facile synthesis of uniform metal carbide nanoparticles from metal-organic frameworks by laser metallurgy. *ACS Appl. Mater. Interfaces* 11, 44573–44581

55. Zang, X.N. *et al.* (2019) Laser-sculptured ultrathin transition metal carbide layers for energy storage and energy harvesting applications. *Nat. Commun.* 10, 3112

56. Zhang, D.S. *et al.* (2019) Carbon-encapsulated metal/metal carbide/metal oxide core-shell nanostructures generated by laser ablation of metals in organic solvents. *ACS Appl. Nano Mater.* 2, 28–39

57. Zelepukin, I.V. *et al.* (2021) Laser-synthesized TiN nanoparticles for biomedical applications: evaluation of safety, biodistribution and pharmacokinetics. *Mater. Sci. Eng. C* 120, 111717

58. Mahjouri-Samani, M. *et al.* (2014) Digital transfer growth of patterned 2D metal chalcogenides by confined nanoparticle evaporation. *ACS Nano* 8, 11567–11575

59. Pasti, I.A. *et al.* (2019) Atomically thin metal films on foreign substrates: from lattice mismatch to electrocatalytic activity. *ACS Catal.* 9, 3467–3481

60. Ou, G. *et al.* (2018) Defective molybdenum sulfide quantum dots as highly active hydrogen evolution electrocatalysts. *Nano Res.* 11, 751–761

61. Sun, X.C. *et al.* (2020) Laser-ablation-produced cobalt nickel phosphate with high-valence nickel ions as an active catalyst for the oxygen evolution reaction. *Chem-Eur. J.* 26, 2793–2797

62. Tang, Y.J. *et al.* (2021) Laser-induced annealing of metal-organic frameworks on conductive substrates for electrochemical water splitting. *Adv. Funct. Mater.* 31, 2102648

63. Zhang, J.B. *et al.* (2018) Oxidized laser-induced graphene for efficient oxygen electrocatalysis. *Adv. Mater.* 30, 1707319

64. Zhang, J.B. *et al.* (2018) *In situ* synthesis of efficient water oxidation catalysts in laser-induced graphene. *ACS Energy Lett.* 3, 677–683

65. Ye, R.Q. *et al.* (2015) *In situ* formation of metal oxide nanocrystals embedded in laser-induced graphene. *ACS Nano* 9, 9244–9251

66. Han, X. *et al.* (2018) Laser-induced graphene from wood impregnated with metal salts and use in electrocatalysis. *ACS Appl. Nano Mater.* 1, 5053–5061

67. Xu, S.M. *et al.* (2019) Uniform, scalable, high-temperature microwave shock for nanoparticle synthesis through defect engineering. *Matter* 1, 759–769

68. Zhong, G. *et al.* (2019) Rapid, high-temperature, *in situ* microwave synthesis of bulk nanocatalysts. *Small* 15, 1904881

69. Gedye, R. *et al.* (1986) The use of microwave-ovens for rapid organic-synthesis. *Tetrahedron Lett.* 27, 279–282

70. Voiry, D. *et al.* (2016) High-quality graphene via microwave reduction of solution-exfoliated graphene oxide. *Science* 353, 1413–1416

71. Chen, W.F. *et al.* (2010) Preparation of graphene by the rapid and mild thermal reduction of graphene oxide induced by microwaves. *Carbon* 48, 1146–1152

72. Huang, H.W. *et al.* (2020) Rapid and energy-efficient microwave pyrolysis for high-yield production of highly-active bifunctional electrocatalysts for water splitting. *Energy Environ. Sci.* 13, 545–553

73. Huang, H.W. *et al.* (2019) Microwave-assisted ultrafast synthesis of molybdenum carbide nanoparticles grown on carbon matrix for efficient hydrogen evolution reaction. *Small Methods* 3, 1900259

74. Barman, B.K. and Nanda, K.K. (2018) Ultrafast-versatile-domestic-microwave-oven based graphene oxide reactor for the synthesis of highly efficient graphene based hybrid electrocatalysts. *ACS Sustain. Chem. Eng.* 6, 4037–4045

75. Gao, T.T. *et al.* (2021) Ultra-fast preparing carbon nanotube-supported trimetallic Ni, Ru, Fe heterostructures as robust bifunctional electrocatalysts for overall water splitting. *Chem. Eng. J.* 424, 130416

76. Zhao, H. *et al.* (2021) Ultrafast generation of nanostructured noble metal aerogels by a microwave method for electrocatalytic hydrogen evolution and ethanol oxidation. *ACS Appl. Nano Mater.* 4, 11221–11230

77. Qiao, H.Y. *et al.* (2021) Scalable synthesis of high entropy alloy nanoparticles by microwave heating. *ACS Nano* 15, 14928–14937

78. Kheradmandfard, M. *et al.* (2021) Ultrafast green microwave-assisted synthesis of high-entropy oxide nanoparticles for Li-ion battery applications. *Mater. Chem. Phys.* 262, 124265

79. Choi, Y. *et al.* (2021) Transformation of microwave synthesized highly uniform FeMo-MIL-88B nanorod to oxynitride derivate for overall water splitting reaction. *Appl. Mater. Today* 24, 101093

80. Barforoush, J.M. *et al.* (2017) Microwave-assisted synthesis of a nanoamorphous (Ni-0.8,Fe-0.2) oxide oxygen-evolving electrocatalyst containing only "fast" sites. *J. Mater. Chem. A* 5, 11661–11670

81. Yan, K.L. *et al.* (2019) Microwave synthesis of ultrathin nickel hydroxide nanosheets with iron incorporation for electrocatalytic water oxidation. *ACS Appl. Energy Mater.* 2, 1961–1968

82. Sarwar, S. *et al.* (2020) Facile microwave approach towards high performance MoS2/graphene nanocomposite for hydrogen evolution reaction. *Sci. China Mater.* 63, 62–74

83. Souleymen, R. *et al.* (2018) Microwave-assisted synthesis of graphene-like cobalt sulfide freestanding sheets as an efficient bifunctional electrocatalyst for overall water splitting. *J. Mater. Chem. A* 6, 7592–7607

84. Youn, D.H. *et al.* (2015) Ultrafast synthesis of MoS_2 or WS_2-reduced graphene oxide composites via hybrid microwave annealing for anode materials of lithium ion batteries. *J. Power Sources* 295, 228–234

85. Morozan, A. *et al.* (2020) Nonprecious bimetallic iron-molybdenum sulfide electrocatalysts for the hydrogen evolution reaction in proton exchange membrane electrolyzers. *ACS Catal.* 10, 14336–14348

86. Wang, B. *et al.* (2022) Nitrogen doped porous carbon polyhedral supported Fe and Ni dual-metal single-atomic catalysts: template-free and metal ligand-free synthesis with microwave-assistance and d-band center modulating for boosted ORR catalysis in zinc-air batteries. *Chem. Eng. J.* 437, 135295

87. Cheng, Y. *et al.* (2019) Unsaturated edge-anchored Ni single atoms on porous microwave exfoliated graphene oxide for electrochemical CO_2. *Appl. Catal. B-Environ.* 243, 294–303

88. Lu, B.Z. *et al.* (2020) Electrocatalysis of single-atom sites: impacts of atomic coordination. *ACS Catal.* 10, 7584–7618

89. Fei, H.L. *et al.* (2015) Atomic cobalt on nitrogen-doped graphene for hydrogen generation. *Nat. Commun.* 6, 8668

90. Gong, H.S. *et al.* (2022) Low-coordinated Co-N-C on oxygenated graphene for efficient electrocatalytic H_2O_2 production. *Adv. Funct. Mater.* 32, 2106886

91. Nie, N.Z. *et al.* (2021) Superfast synthesis of densely packed and ultrafine Pt-lanthanide@KB via solvent-free microwave as efficient hydrogen evolution electrocatalysts. *Small* 17, 2102879

92. Furukawa, S. and Komatsu, T. (2017) Intermetallic compounds: promising inorganic materials for well-structured and electronically modified reaction environments for efficient catalysis. *ACS Catal.* 7, 735–765

93. Ryoo, R. *et al.* (2020) Rare-earth-platinum alloy nanoparticles in mesoporous zeolite for catalysis. *Nature* 585, 221–224

94. Wu, X.K. *et al.* (2021) Solvent-free microwave synthesis of ultrasmall Ru-Mo2C@CNT with strong metal-support interaction for industrial hydrogen evolution. *Nat. Commun.* 12, 4018

95. Lucia, O. *et al.* (2014) Induction heating technology and its applications: past developments, current technology, and future challenges. *IEEE T. Ind. Electron.* 61, 2509–2520

96. Wang, W. *et al.* (2019) Induction heating: an enabling technology for the heat management in catalytic processes. *ACS Catal.* 9, 7921–7935

97. Zhao, T. *et al.* (2019) Ultrafast growth of nanocrystalline graphene films by quenching and grain-size-dependent strength and bandgap opening. *Nat. Commun.* 10, 4854

98. Zhang, Y.Q. *et al.* (2016) Rapid synthesis of cobalt nitride nanowires: highly efficient and low-cost catalysts for oxygen evolution. *Angew. Chem. Int. Edit.* 55, 8670–8674

99. Gao, S.J. *et al.* (2020) Synthesis of high-entropy alloy nanoparticles on supports by the fast moving bed pyrolysis. *Nat. Commun.* 11, 2016

100. Guo, Y.B. *et al.* (2022) Nickel single-atom catalysts intrinsically promoted by fast pyrolysis for selective electroreduction of CO_2 into CO. *Appl. Catal. B-Environ.* 304, 120997